Title

Statistical properties of plasmaspheric hiss derived from Van Allen Probes data and their Effects on radiation belt electron dynamics

Journal

Journal of Geophysical Research A: Space Physics, 120(5)

ISSN

2169-9380

Authors

Li, W
Ma, Q
Thorne, RM
et al.

Publication Date

2015

DOI

10.1002/2015JA021048

Peer reviewed

AGU PUBLICATIONS

JGR

Journal of Geophysical Research: Space Physics

RESEARCH ARTICLE
10.1002/2015JA021048

Special Section:
Low-Frequency Waves in Space Plasmas

Statistical properties of plasmaspheric hiss derived from Van Allen Probes data and their effects on radiation belt electron dynamics

W. Li[1], Q. Ma[1], R. M. Thorne[1], J. Bortnik[1], C. A. Kletzing[2], W. S. Kurth[2], G. B. Hospodarsky[2], and Y. Nishimura[1]

[1]Department of Atmospheric and Oceanic Sciences, UCLA, Los Angeles, California, USA, [2]Department of Physics and Astronomy, University of Iowa, Iowa City, Iowa, USA

Key Points:
- Hiss wave power is activity dependent and frequently extends below 100 Hz
- Hiss peak frequency is dependent on L and lower than the previous value 550 Hz
- Difference in hiss diffusion rate is up to 5, and realistic spectra should be used

Correspondence to:
W. Li,
moonli@atmos.ucla.edu

Citation:
Li, W., Q. Ma, R. M. Thorne, J. Bortnik, C. A. Kletzing, W. S. Kurth, G. B. Hospodarsky, and Y. Nishimura (2015), Statistical properties of plasmaspheric hiss derived from Van Allen Probes data and their effects on radiation belt electron dynamics, *J. Geophys. Res. Space Physics*, *120*, 3393–3405, doi:10.1002/2015JA021048.

Received 23 JAN 2015
Accepted 2 APR 2015
Accepted article online 7 APR 2015
Published online 6 MAY 2015

Abstract Plasmaspheric hiss is known to play an important role in controlling the overall structure and dynamics of radiation belt electrons inside the plasmasphere. Using newly available Van Allen Probes wave data, which provide excellent coverage in the entire inner magnetosphere, we evaluate the global distribution of the hiss wave frequency spectrum and wave intensity for different levels of substorm activity. Our statistical results show that observed hiss peak frequencies are generally lower than the commonly adopted value (~550 Hz), which was in frequent use, and that the hiss wave power frequently extends below 100 Hz, particularly at larger L shells ($>$ ~3) on the dayside during enhanced levels of substorm activity. We also compare electron pitch angle scattering rates caused by hiss using the new statistical frequency spectrum and the previously adopted Gaussian spectrum and find that the differences are up to a factor of ~5 and are dependent on energy and L shell. Moreover, the new statistical hiss wave frequency spectrum including wave power below 100 Hz leads to increased pitch angle scattering rates by a factor of ~1.5 for electrons above ~100 keV at L~5, although their effect is negligible at $L \leq 3$. Consequently, we suggest that the new realistic hiss wave frequency spectrum should be incorporated into future modeling of radiation belt electron dynamics.

1. Introduction

Plasmaspheric hiss is a structureless and broadband whistler mode emission typically observed inside the plasmasphere [*Dunckel and Helliwell*, 1969; *Thorne et al.*, 1973; *Meredith et al.*, 2004] and high-density plumes in the Earth's magnetosphere [*Chan and Holzer*, 1976; *Parrot and Lefeuvre*, 1986; *Summers et al.*, 2008]. Plasmaspheric hiss causes electron precipitation into the upper atmosphere through pitch angle scattering over a broad range of energies from tens of keV to a few MeV on time scales ranging from days to weeks and thus plays a vital role in controlling radiation belt electron dynamics [*Lyons and Thorne*, 1973; *Abel and Thorne*, 1998a, 1998b; *Meredith et al.*, 2006, 2007, 2009; *Thorne et al.*, 2013]. Specifically, plasmaspheric hiss can account for efficient electron precipitation from tens to hundreds of keV in the outer plasmasphere [e.g., *Li et al.*, 2014] and is also responsible for the gradual decay of the recently reported "unusual narrow ring" of ~MeV electrons in the radiation belts [*Baker et al.*, 2013; *Thorne et al.*, 2013].

Although the wave frequency spectrum of plasmaspheric hiss has been studied using previous satellite data (i.e., CRRES and Polar) [e.g., *Meredith et al.*, 2004; *Tsurutani et al.*, 2015], the statistical results still need further improvement due to the following reasons. First, CRRES wave measurements were limited to wave frequencies above ~100 Hz. However, a recent observation by the Van Allen Probes [e.g., *Li et al.*, 2013] and the Polar satellite [*Tsurutani et al.*, 2015] reported low-frequency plasmaspheric hiss, which contained much lower frequencies extending down to ~20 Hz. Second, statistical results from CRRES have a limited spatial coverage with a gap on the dayside, where plasmaspheric hiss is typically strong. Third, wave magnetic amplitudes from CRRES were inferred from wave electric field measurements by assuming that waves propagate parallel to the background magnetic field, even though the realistic wave normal distributions of plasmaspheric hiss are highly variable [e.g., *Parrot and Lefeuvre*, 1986; *Santolík et al.*, 2001; *Bortnik et al.*, 2011; *Agapitov et al.*, 2013]. Last but not least, without wave polarization properties, it was difficult to differentiate hiss from other types of emissions in the inner magnetosphere. Although statistical results from the Polar spacecraft [*Tsurutani et al.*, 2015] overcame some of the limitations inherent in the CRRES statistics, the time period over which Polar data were collected lasted 1 year (1996–1997), it was at

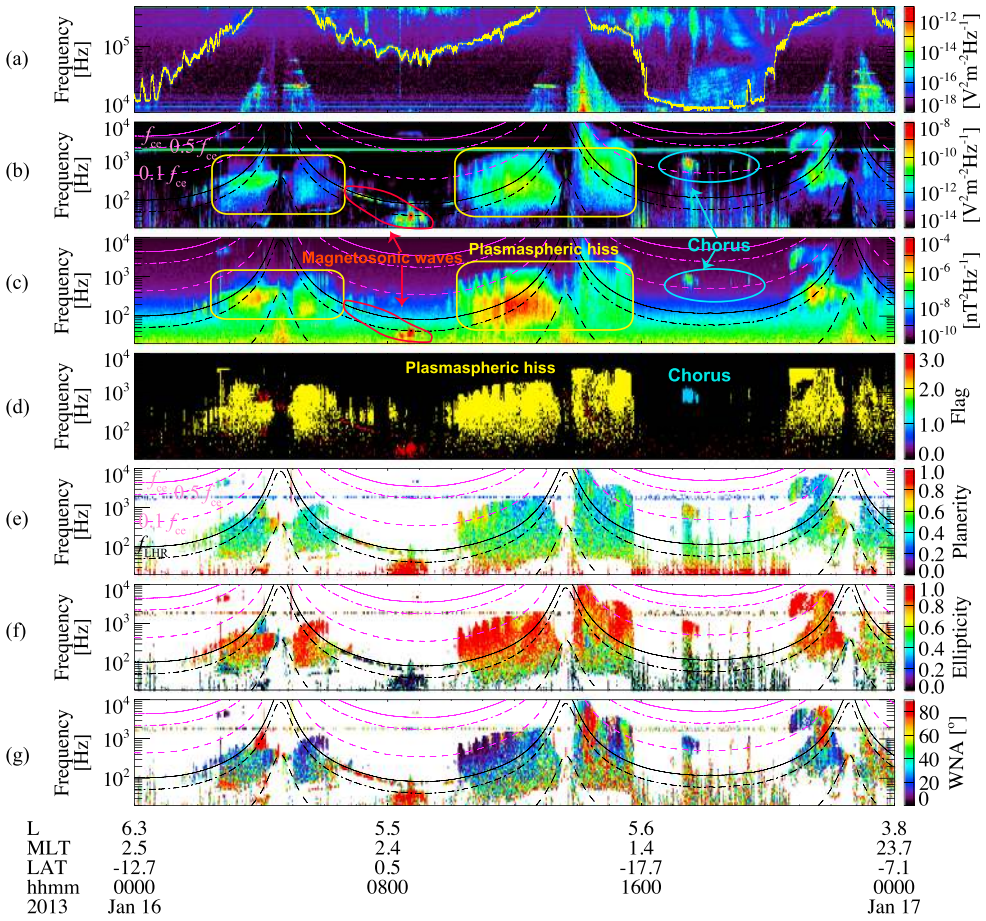

Figure 1. A wave survey plot showing various magnetospheric waves observed by Van Allen Probe A. (a) Frequency-time spectrogram of electric field spectral intensity measured by HFR, and the yellow line represents the detected upper hybrid resonance frequency. (b) Frequency-time spectrogram of wave spectral intensity in electric field and (c) magnetic field observed by WFR. (d) A flag indicating the wave type, where yellow (Flag = 2), light blue (Flag = 1), and dark red colors (Flag = 3) represent plasmaspheric hiss, chorus, and magnetosonic waves, respectively. (e) Frequency-time spectrogram of planarity, (f) ellipticity, and (g) wave normal angles. In Figures 1b–1g, the solid, dash-dotted, and dashed magenta lines indicate f_{ce}, 0.5 f_{ce}, and 0.1 f_{ce}, where f_{ce} is the electron cyclotron frequency; the solid, dash-dotted, and dashed black lines represent f_{LHR}, 0.5 f_{LHR}, and f_{ci}, where f_{LHR} is the lower hybrid resonance frequency and f_{ci} is the proton cyclotron frequency.

solar minimum with a lack of intense geomagnetic storms [e.g., *Tsurutani et al.*, 2006], and Polar spacecraft generally spent a short fraction of its orbital period near the equatorial region. Complementary to the CRRES and Polar statistics, Van Allen Probes wave measurements provide an unprecedented opportunity for statistically evaluating wave spectral properties due to the availability of both electric and magnetic wavefield measurements together with the polarization properties, broader wave frequency coverage, and extensive spatial coverage over the entire inner magnetosphere ($L < 6$) near the equatorial region. Therefore, Van Allen Probes wave data are ideally suited to provide significantly improved statistical results of plasmaspheric hiss wave intensity and wave frequency spectrum.

To evaluate the effects of plasmaspheric hiss on energetic electron dynamics, a Gaussian wave frequency spectrum with a peak frequency of ~550 Hz and frequency bandwidth of ~300 Hz has been frequently adopted over the range of wave frequencies between 100 Hz and 2 kHz [*Lyons et al.*, 1972; *Summers et al.*, 2007; *Shprits et al.*, 2009; *Thorne et al.*, 2013; *Ni et al.*, 2013, 2014]. However, a case study using Van Allen Probes wave observations by *Ni et al.* [2014] showed that the observed hiss wave spectrum could be significantly different from this Gaussian distribution and this difference in the wave frequency spectrum has been shown to considerably affect electron scattering rates in a selected electron energy range.

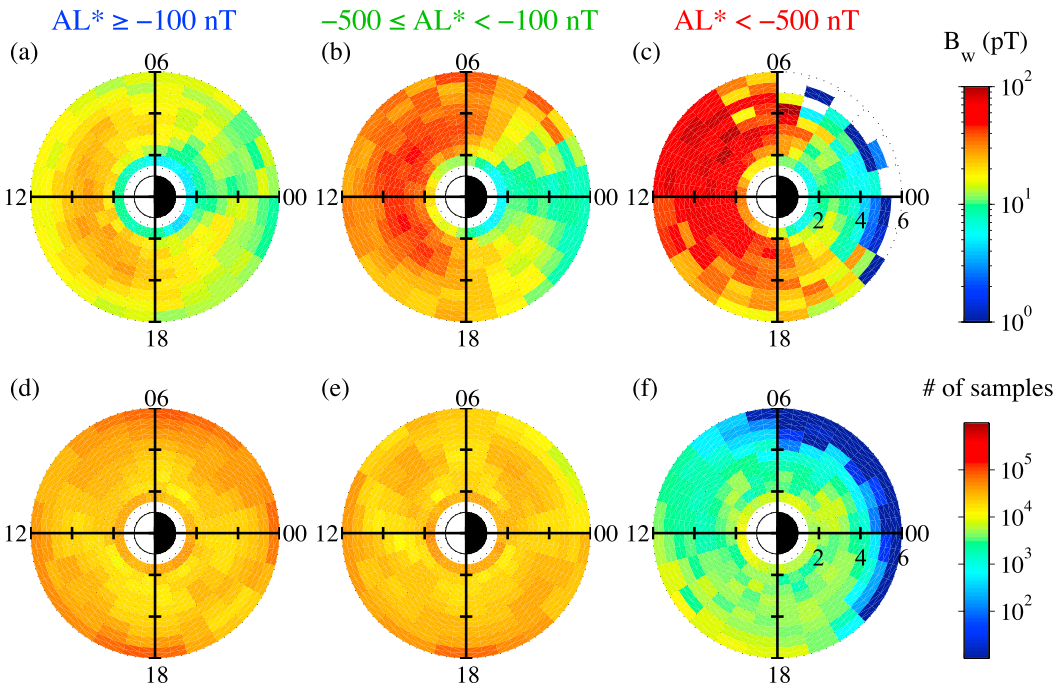

Figure 2. (a–c) Global distribution of hiss wave amplitudes in the *L*-MLT domain during quiet ($AL^* \geq -100$ nT), modestly disturbed ($-500 \leq AL^* < -100$ nT), and active ($AL^* < -500$ nT) times. (d–f) The same as Figures 2a–2c but for the number of samples collected in each 0.5 $L \times 1$ h (MLT) bin.

Meredith et al. [2007, 2009] carefully examined the spectral distribution of plasmaspheric hiss using CRRES data and obtained more accurate fits to the wave data over the frequency range of 100 Hz–5 kHz by adding together three Gaussian distributions. These fitted frequency spectra have been used in the British Antarctic Survey Radiation Belt Model [*Glauert et al.*, 2014] for modeling and forecasting applications. *Meredith et al.* [2007, 2009] found that in the region of $2 < L < 4$, the peak frequencies of plasmaspheric hiss lie in the range of 173–366 Hz during active conditions, which is much lower than the frequently adopted peak frequency of 550 Hz, but still excludes the wave power below 100 Hz.

Since it is crucial to obtain realistic hiss wave spectral properties in order to accurately evaluate the role of plasmaspheric hiss in energetic electron precipitation at various energies, in the present study, we evaluate the global distribution of hiss wave intensities and wave frequency spectra and their dependence on *L* shell, magnetic local time (MLT), and substorm activity using 2 years of Van Allen Probes wave data. We also determine the difference in electron pitch angle scattering rates using the wave spectral model of plasmaspheric hiss from our new statistical result and the previously frequently used Gaussian spectrum. Finally, we quantify the role of low-frequency hiss (<100 Hz) in electron pitch angle scattering rates to evaluate the importance of including this previously neglected frequency component.

2. Van Allen Probes Wave Data Analysis

Plasmaspheric hiss wave properties were analyzed using the Electric and Magnetic Field Instrument Suite and Integrated Science (EMFISIS) [*Kletzing et al.*, 2013] wave data recorded by the twin Van Allen Probes with an apogee of ~5.8 R_E [*Mauk et al.*, 2012]. The waveform receiver (WFR) on the EMFISIS Waves instruments provides both wave power spectral density and wave polarization properties including wave normal angle, ellipticity, and planarity calculated by the singular value decomposition method [*Santolík et al.*, 2003] over the frequency range from 10 Hz up to ~12 kHz. The high-frequency receiver (HFR) measures electric spectral intensity between 10 and ~400 kHz, from which the upper hybrid resonance frequency can be identified and used to calculate the total plasma density [*Kurth et al.*, 2015]. This inferred total plasma density is used to determine whether the satellite is located in the plasmaspheric or plasmatrough-like

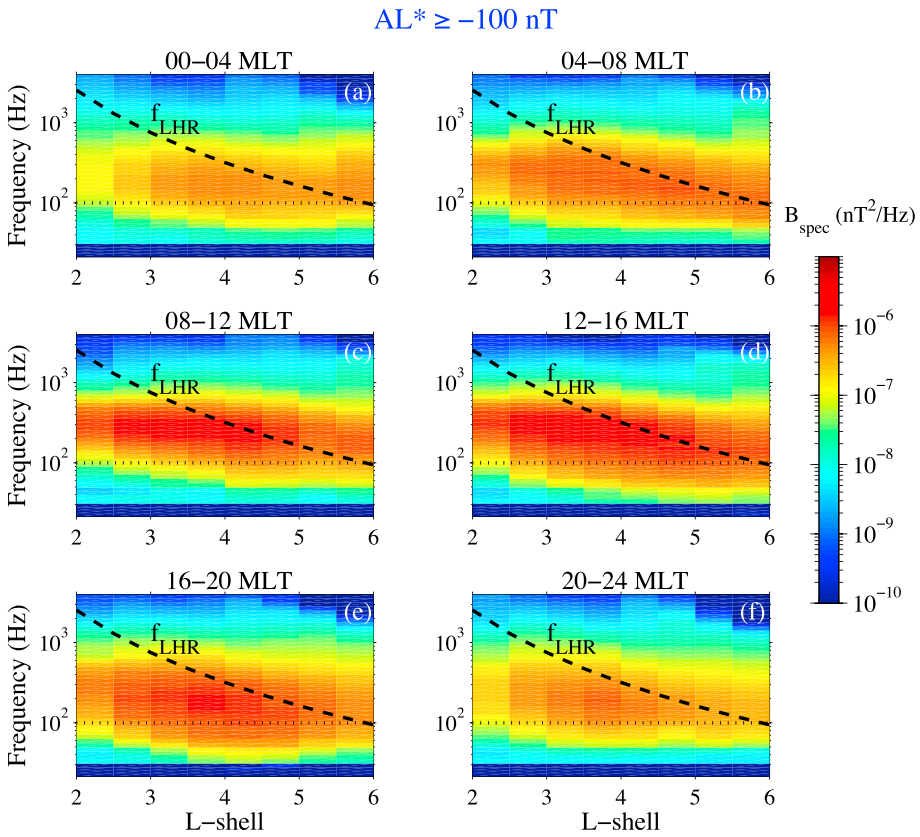

Figure 3. Hiss magnetic wave spectral density as a function of L shell and frequency during quiet times ($AL^* \geq -100$ nT) in various MLT sectors. Here the black dashed line represents f_{LHR}, and the dotted line indicates the constant frequency at 100 Hz, which is the lower cutoff frequency in the CRRES statistics.

region. Specifically, if the in situ plasma density is higher than the larger value between $10 \times (6.6/L)^4$ and 50 cm^{-3}, the region is defined to be a plasmaspheric region; otherwise, it is taken to be a plasmatrough-like region, following the method used in *Li et al.* [2010]. As illustrated in Figure 1, in our hiss wave data set, we only included waves over the frequency range of 20–4000 Hz in the plasmaspheric region with planarity larger than 0.2 (Figure 1e) and ellipticity (Figure 1f) larger than 0.7 and set the time-frequency bin satisfying these criteria to a flag equal to 2 (yellow region in Figure 1d). By doing so, we excluded chorus waves typically observed in the plasmatrough region with frequencies between 0.1 and 0.8 f_{ce}, where f_{ce} is the electron cyclotron frequency [e.g., *Burtis and Helliwell*, 1969; *Burton and Holzer*, 1974; *Tsurutani and Smith*, 1974, 1977; *Meredith et al.*, 2003, 2012; *Li et al.*, 2009, 2011]. We further excluded magnetosonic waves by removing waves with frequencies below the lower hybrid resonance frequency having wave normal angles (Figure 1g) larger than 80° and ellipticity (Figure 1f) between −0.2 and 0.2, since magnetosonic waves typically have wave normal angles close to ~90° and very low ellipticity near 0 [e.g., *Horne et al.*, 2007]. In the example shown in Figure 1, our algorithm clearly identifies plasmaspheric hiss among various types of waves including chorus (light blue), hiss (yellow), and magnetosonic waves (dark red), as explicitly shown by the flags indicating wave type (Figure 1d).

3. Statistical Results From Van Allen Probes Wave Data

Van Allen Probes EMFISIS wave data from 1 October 2012 to 1 October 2014 have been used to perform a statistical analysis of the hiss wave amplitudes and wave frequency spectra. The EMFISIS wave data have been collected near the equatorial inner magnetosphere mostly within 20° of the magnetic equator. Figure 2 shows the global distribution of time-averaged root-mean-square (RMS) values of hiss wave amplitudes (integrated over the frequency range from 20 Hz to 4 kHz) in the L-MLT domain. Here L shell is

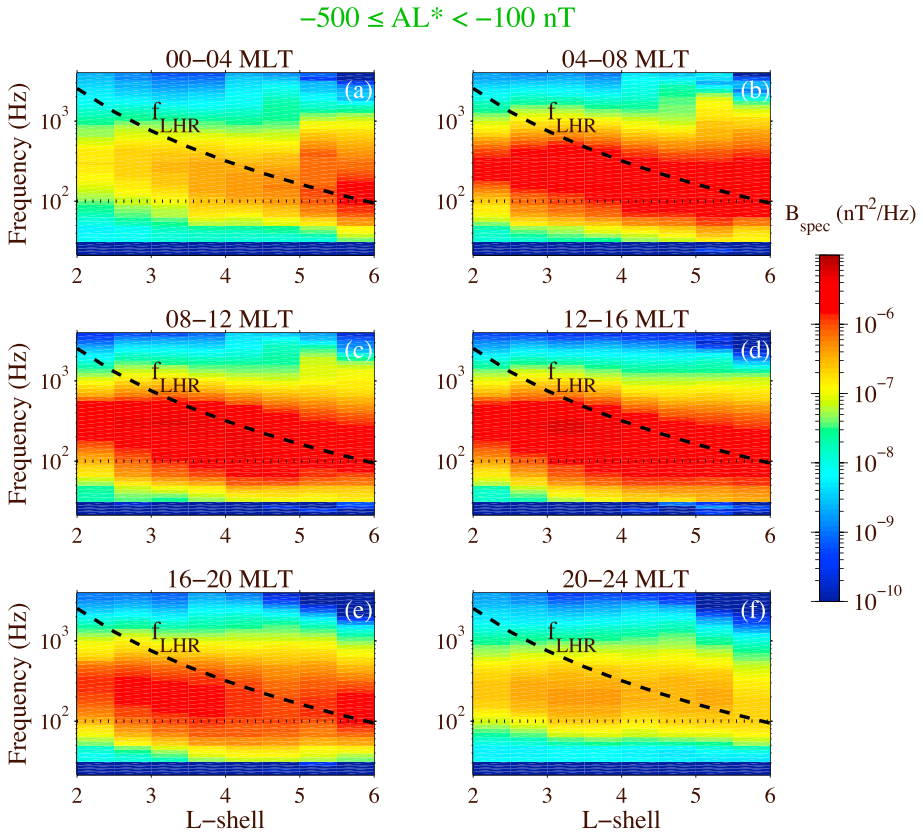

Figure 4. The same as Figure 3 but during modestly disturbed times ($-500 \leq AL^* < -100$ nT).

defined as the geocentric distance to the point with minimum magnetic field intensity using the TS04D magnetic field model [*Tsyganenko and Sitnov*, 2005] for the field line threading the satellite. These plasmaspheric hiss waves were observed either inside the plasmasphere or within plasmaspheric plumes, as long as the plasma density at the satellite location was higher than the larger value between $10 \times (6.6/L)^4$ and $50\,\mathrm{cm}^{-3}$. We evaluate the hiss wave distribution with respect to substorm activity, following *Meredith et al.* [2004], but use *AL* rather than *AE*, since *AL* is known to be more directly related to substorm activity [e.g., *McPherron et al.*, 2013]. We sorted the wave distribution into quiet ($AL^* \geq -100$ nT), moderately disturbed ($-500 \leq AL^* < -100$ nT), and active ($AL^* < -500$ nT) times, where *AL** is the minimum *AL* in the previous 3 h. We used *AL** rather than the instantaneous *AL* following previous studies, since the maximum *AE* in the preceding 3 h (*AE**) has been shown to be better than the instantaneous *AE* to sort the wave intensity by taking into account the drift time of electrons with energies from tens to hundreds of keV [*Meredith et al.*, 2004, 2007], which are relevant to hiss wave amplification or chorus excitation which then evolves into hiss [*Bortnik et al.*, 2008, 2009; *Chen et al.*, 2012; *Li et al.*, 2015]. Two years of Van Allen Probes wave data provide excellent coverage over all MLT sectors in the entire inner magnetosphere, as shown by the number of samples in Figures 2d–2f. Hiss wave amplitudes (Figures 2a–2c) increase on the dayside as the level of substorm activity increases (*AL** decreases), while it decreases on the nightside as the substorm activity increases. This is probably because during active times, suprathermal electron fluxes are larger on the nightside, which causes stronger Landau damping of whistler mode waves [*Bortnik et al.*, 2007; *Li et al.*, 2010] and thus limits the ability of chorus waves to propagate into the plasmasphere and evolve into plasmaspheric hiss [e.g., *Bortnik et al.*, 2008, 2009; *Li et al.*, 2015]. The RMS hiss wave amplitudes peak at ~20 pT during quiet times on the dayside (Figure 2a), increase to 40–50 pT during moderately disturbed times (Figure 2b), and reach up to a couple of hundred pT during active times (Figure 2c). The overall trend of our new global distribution of plasmaspheric hiss wave intensity is roughly consistent with the CRRES statistics [e.g., *Meredith et al.*, 2007]. However, the hiss wave intensity distribution

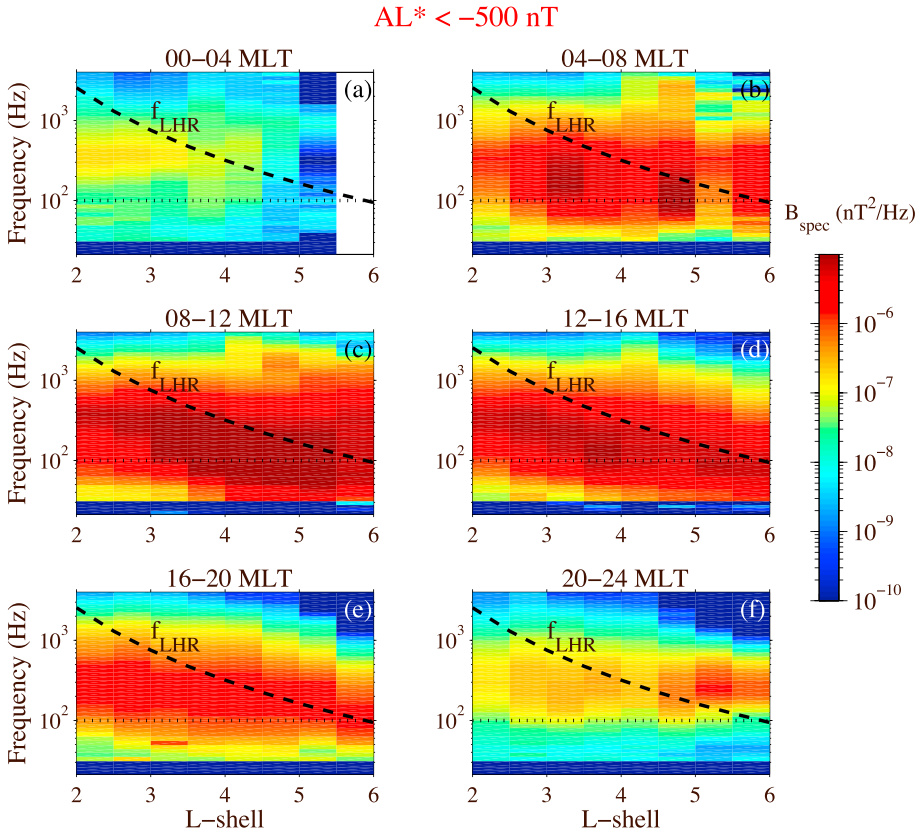

Figure 5. The same as Figure 3 but during active times ($AL^* < -500$ nT).

from our statistical results is smoother and more complete than the CRRES results due to the extensive data coverage from two Van Allen Probes over 2 years.

We also sorted the global distribution of hiss wave intensity into two different magnetic latitude (MLAT) regions: $|\text{MLAT}| < 10°$ and $|\text{MLAT}| \geq 10°$ (not shown). However, their distributions in these two different regions are quite similar using Van Allen Probes wave data, which were mostly collected over $|\text{MLAT}| < 20°$. This is consistent with the Polar statistics [*Tsurutani et al.*, 2015], where the variation in hiss occurrence rate was found to be insignificant over $|\text{MLAT}| < 20°$.

We performed a statistical analysis of hiss wave frequency spectra and categorized them into three levels of substorm activity. Statistical results of hiss wave magnetic field spectral intensity during quiet times ($AL^* \geq -100$ nT) are shown as a function of L shell and frequency in Figure 3 in six different MLT sectors. During quiet times, the hiss wave intensities exhibit a weak dependence on MLT. The peak frequency of hiss wave spectral intensity is almost constant and mostly above 100 Hz at $L < 3$. At larger L shells (>3), the peak wave frequency tends to slightly decrease, and the wave power extends below 100 Hz. Note that 100 Hz was the lower cutoff frequency from the CRRES database and was also the frequently adopted lower cutoff frequency in previous modeling studies [e.g., *Lyons et al.*, 1972; *Summers et al.*, 2007; *Shprits et al.*, 2009; *Ni et al.*, 2013, 2014; *Thorne et al.*, 2013]. Figure 4 shows the hiss wave frequency spectra with the same format as Figure 3 but during moderately active conditions ($-500 \leq AL^* < -100$ nT). The MLT dependence of hiss wave intensities becomes more pronounced during more active times with the larger wave spectral intensity over 04:00–20:00 MLT compared to that over 20:00–04:00 MLT. Hiss wave power also extends below 100 Hz over 04:00–20:00 MLT at larger L shells (> ~3). Furthermore, while the peak frequency clearly does not follow f_{LHR} at $L <$ ~3, it does tend to follow f_{LHR} at large L shells (> ~3). Both of the above effects may be related to the injection of tens to hundreds of keV electrons into the outer plasmasphere on the dayside in association with substorms, which can cause hiss wave amplification [e.g., *Li et al.*, 2013; *Chen et al.*, 2014]. During active times ($AL^* < -500$ nT), hiss wave spectral intensity becomes even stronger and wave power

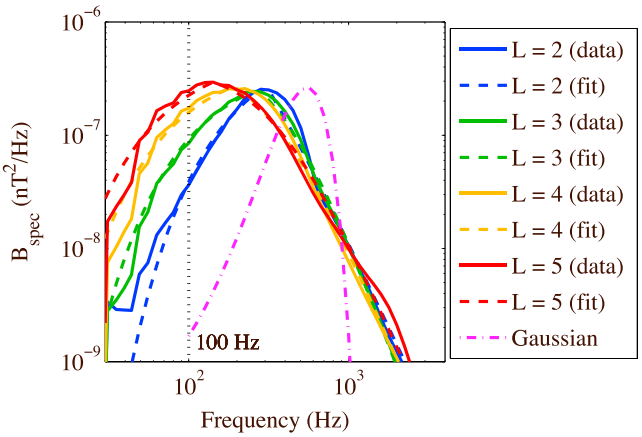

Figure 6. Hiss magnetic wave spectral intensity as a function of wave frequency shown at various *L* shells (color coded). Here the solid lines indicate the statistical hiss wave frequency spectra at each corresponding *L* shell, and the dashed lines represent the fitted curves to the statistical results. The dash-dotted magenta line represents the frequently adopted Gaussian wave frequency spectrum, and the vertical dotted black line is the constant frequency of 100 Hz.

extends well below 100 Hz on the dayside (04:00–16:00 MLT) at $L > \sim 3$, as shown in Figure 5. In contrast, on the nightside (Figures 5a and 5f), the wave spectral intensity is much lower and is mostly above 100 Hz. These statistical results clearly show that plasmaspheric hiss with frequencies below 100 Hz is not unusual and preferentially occurs in the outer plasmasphere on the dayside during periods of modest to strong substorm activity.

We evaluated the dependence of the normalized hiss wave frequency spectrum on *L* shell, MLT, and *AL**, as well as the hiss wave amplitude (not shown), and found that the most clear dependence is on *L* shell. Therefore, in Figure 6, we show magnetic wave frequency spectra of plasmaspheric hiss averaged over all MLT sectors and geomagnetic activity levels but sorted into different *L* shells (color coded) with solid (dashed) lines representing the statistical result (fitted curve). The dash-dotted magenta line shows the previously frequently used Gaussian frequency distribution [e.g., *Meredith et al.*, 2006; *Summers et al.*, 2007; *Thorne et al.*, 2013; *Ni et al.*, 2013, 2014], which is expressed in terms of $\exp\left[-\left(\frac{f-f_m}{\Delta f}\right)^2\right]$ with the wave frequency corresponding to the maximum wave spectral density $f_m = 550$ Hz, the frequency width $\Delta f = 300$ Hz, and the lower and upper cutoff frequencies at 100 Hz and 2 kHz, respectively. These frequency distributions are normalized to the same hiss wave amplitude of 10 pT for both the statistical and the Gaussian spectra. The hiss wave frequency distribution from our new statistical result is clearly different from the previous Gaussian distribution. First, the peak frequency lies between 100 and 300 Hz, which is much smaller than 550 Hz, and the peak frequency decreases as the *L* shell increases. This is consistent with the previous CRRES statistical result showing a peak frequency over 173–366 Hz in the region of $2 < L < 4$ [*Meredith et al.*, 2007, 2009]. Second, the hiss wave power extends well below 100 Hz particularly at larger *L* shells. Third, the wave power above 1 kHz is stronger than that from the Gaussian spectrum. These new statistical results clearly suggest that the frequently adopted Gaussian hiss frequency spectrum (with a peak frequency at 550 Hz) needs correction and a more realistic hiss wave frequency spectrum should be incorporated in quantifying hiss-driven electron precipitation.

We performed a least squares fit to the statistical result of hiss wave frequency spectrum at each *L* shell using the following two functions:

$$y(f \le f_{peak}) = c_1 \exp\left(-\frac{df}{f}\right);$$

$$y(f > f_{peak}) = c_2 \left(1 + \frac{f^2}{\kappa t}\right)^{(-\kappa-1)},$$

where *y* is the magnetic wave spectral density (nT^2/Hz), *f* is the wave frequency ranging between 20 and 4000 Hz, f_{peak} is the wave frequency corresponding to the peak spectral intensity, and *df*, κ, *t*, c_1, and c_2 are the fitting parameters. The corresponding fitting parameters are listed in Table 1. As shown in Figure 6, the fitted curves (dashed) match the corresponding statistical results (solid) remarkably well. Since this is the hiss wave frequency spectrum for a fixed wave amplitude (B_w) of 10 pT, hiss wave spectral density with a different wave amplitude can be obtained by scaling the actual wave power (B_w^2). It is important to note that although hiss wave frequency spectrum also varies slightly by geomagnetic activity, MLT, and wave

Table 1. The Fitting Parameters of Hiss Wave Frequency Spectrum at Various *L* Shells

L Shell	f_{peak}	*df*	κ	*t*	c_1	c_2
2	282	290	0.495	5.2e4	7.1e-7	2.7e-6
3	252	160	0.915	1.6e5	4.6e-7	5.6e-7
4	178	110	0.624	1.6e5	4.8e-7	4.5e-7
5	142	90	0.574	2.0e5	5.5e-7	3.8e-7

amplitude, we find that the strongest dependence is on *L* shell. Therefore, the above hiss wave frequency spectra at various *L* shells are representative but simple enough for other scientists to adopt in their future simulations.

4. Pitch Angle Scattering Rates Driven by Various Hiss Wave Frequency Spectra

Bounce-averaged electron pitch angle diffusion coefficients are calculated using the University of California, Los Angeles (UCLA) Full Diffusion Code [e.g., *Ni et al.*, 2008] by including harmonic resonances from −50 to +50 and the Landau resonance. For simplicity, a dipole magnetic field model and the plasmaspheric density model by *Sheeley et al.* [2001] are used to evaluate the magnetic field intensity and plasma density

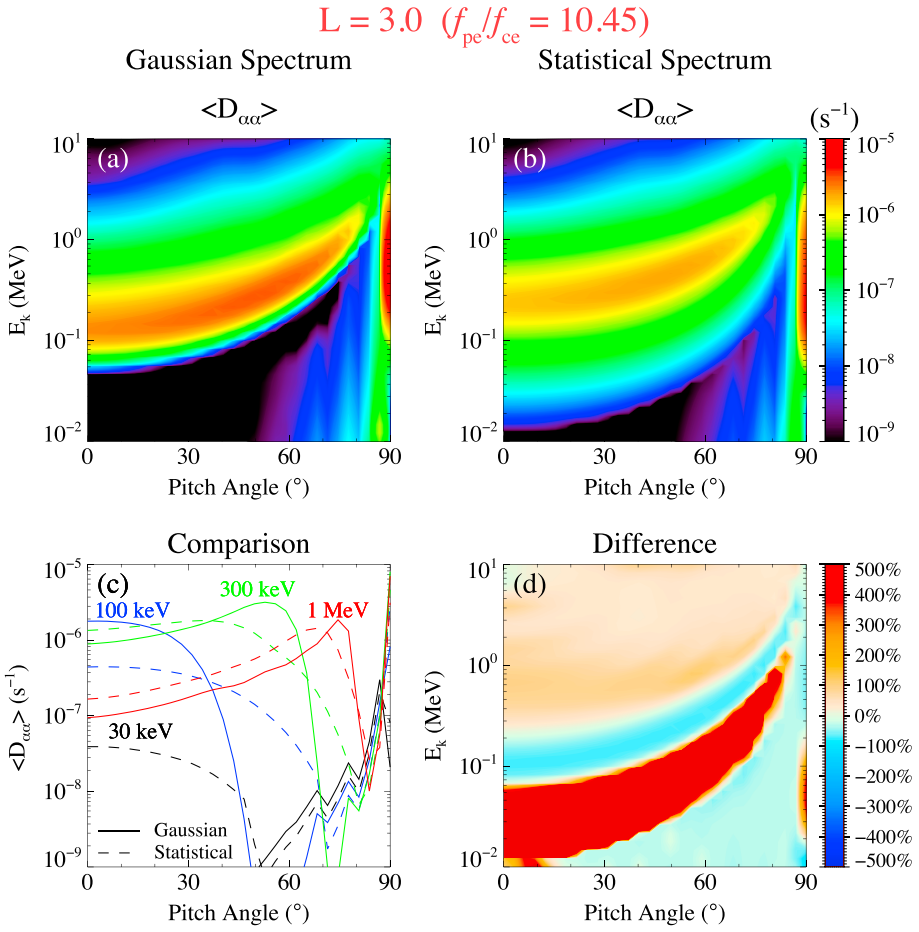

Figure 7. (a) Bounce-averaged pitch angle diffusion coefficients as a function of equatorial pitch angle and energy by using the Gaussian spectrum with the wave amplitudes of 10 pT at $L = 3$, where equatorial f_{pe}/f_{ce} is 10.45. (b) The same as Figure 7a but using the statistical spectrum. (c) Pitch angle diffusion coefficients as a function of equatorial pitch angle for various energies (color coded) for the Gaussian spectrum (solid line) and statistical spectrum (dashed line). (d) The normalized difference of pitch angle diffusion coefficients $\frac{D_{\alpha\alpha}|_{stat} - D_{\alpha\alpha}|_{Gauss}}{D_{\alpha\alpha}|_{Gauss}}$ shown as a function of equatorial pitch angle and energy.

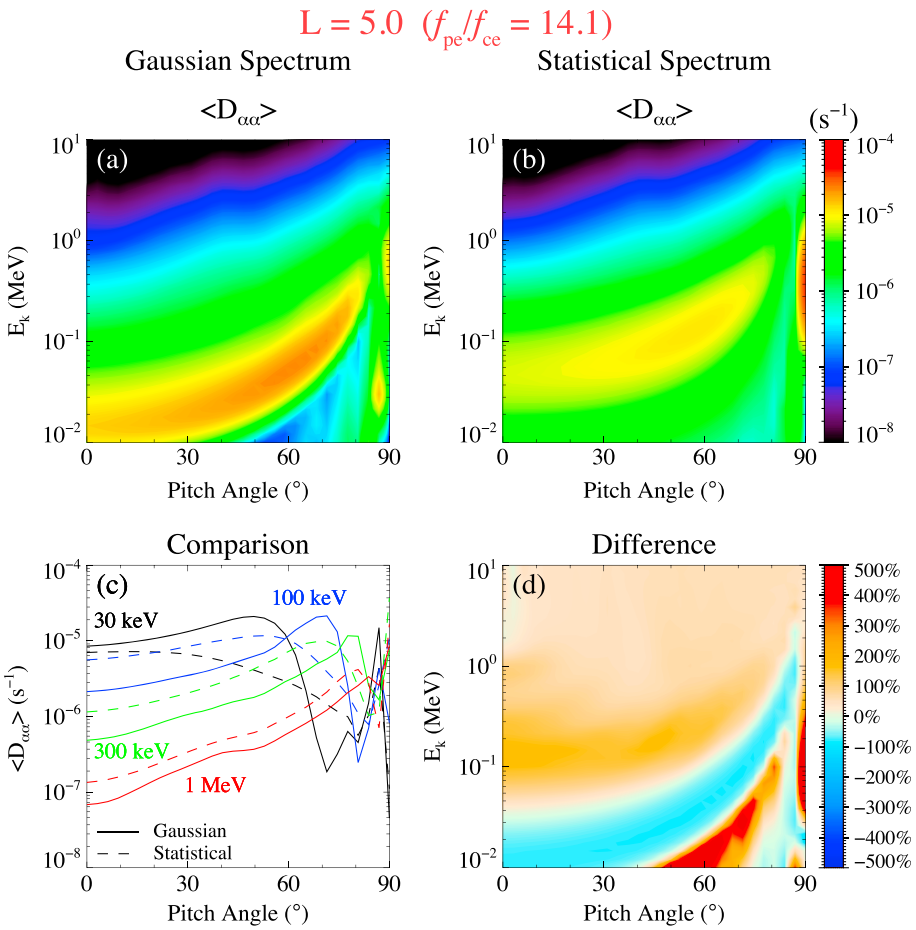

Figure 8. The same as Figure 7 but shown at $L = 5$, where equatorial f_{pe}/f_{ce} is 14.1.

in order to calculate diffusion coefficients. The wave normal angles of plasmaspheric hiss are assumed to increase with latitudes, with field aligned near the magnetic equator and highly oblique at larger latitudes (45°), following *Ni et al.* [2013]. We calculate pitch angle diffusion coefficients separately for the wave frequency spectrum using the Gaussian (dashed magenta line in Figure 6) and statistical distribution (solid line in Figure 6) with the same magnetic wave amplitude of 10 pT by keeping other plasma and wave parameters exactly the same. Figure 7 shows their comparison at $L = 3$, where plasmaspheric hiss plays a critical role in controlling electron dynamics from tens of keV to a few MeV [*Lyons and Thorne*, 1973; *Abel and Thorne*, 1998a, 1998b; *Meredith et al.*, 2006, 2007; *Thorne et al.*, 2013]. The adopted ratio of plasma to electron cyclotron frequency (f_{pe}/f_{ce}) is 10.45 near the equator at $L = 3$. The normalized difference in pitch angle diffusion coefficients using the Gaussian spectrum ($D_{\alpha\alpha}|_{Gauss}$) and statistical spectrum ($D_{\alpha\alpha}|_{Stat}$) is defined as $\frac{D_{\alpha\alpha}|_{Stat} - D_{\alpha\alpha}|_{Gauss}}{D_{\alpha\alpha}|_{Gauss}}$ and is shown in Figure 7d. Here the light green color (~0%) means that $D_{\alpha\alpha}|_{Gauss}$ and $D_{\alpha\alpha}|_{Stat}$ are almost the same, and the warm (cool) color indicates that $D_{\alpha\alpha}|_{Stat}$ is larger (smaller) than $D_{\alpha\alpha}|_{Gauss}$. Near the bounce loss cone within a few degrees of pitch angle, the most pronounced difference is in the energy range of 10–70 keV, where $D_{\alpha\alpha}|_{Stat}$ is larger than $D_{\alpha\alpha}|_{Gauss}$ by a factor of more than 5. However, $D_{\alpha\alpha}|_{Stat}$ is smaller than $D_{\alpha\alpha}|_{Gauss}$ by a factor of ~3 over 70–200 keV. From ~300 keV to ~1 MeV, $D_{\alpha\alpha}|_{Stat}$ is larger than $D_{\alpha\alpha}|_{Gauss}$ by a factor of ~2, as shown in Figure 7c.

Figure 8 is shown with the same format as Figure 7 but at $L = 5$, where the adopted equatorial f_{pe}/f_{ce} is 14.1. At this larger L shell, while the general pattern of differences (Figure 8d) is similar to Figure 7d, it shifts to lower energies due to the higher value of f_{pe}/f_{ce}. Over 10–30 keV, $D_{\alpha\alpha}|_{Stat}$ is smaller than $D_{\alpha\alpha}|_{Gauss}$, but is larger by a factor of ~3 over 70–300 keV, and is slightly larger at a few MeV within a factor of 2. Overall, pitch angle scattering rates of each hiss wave frequency spectrum are quite energy dependent but could have

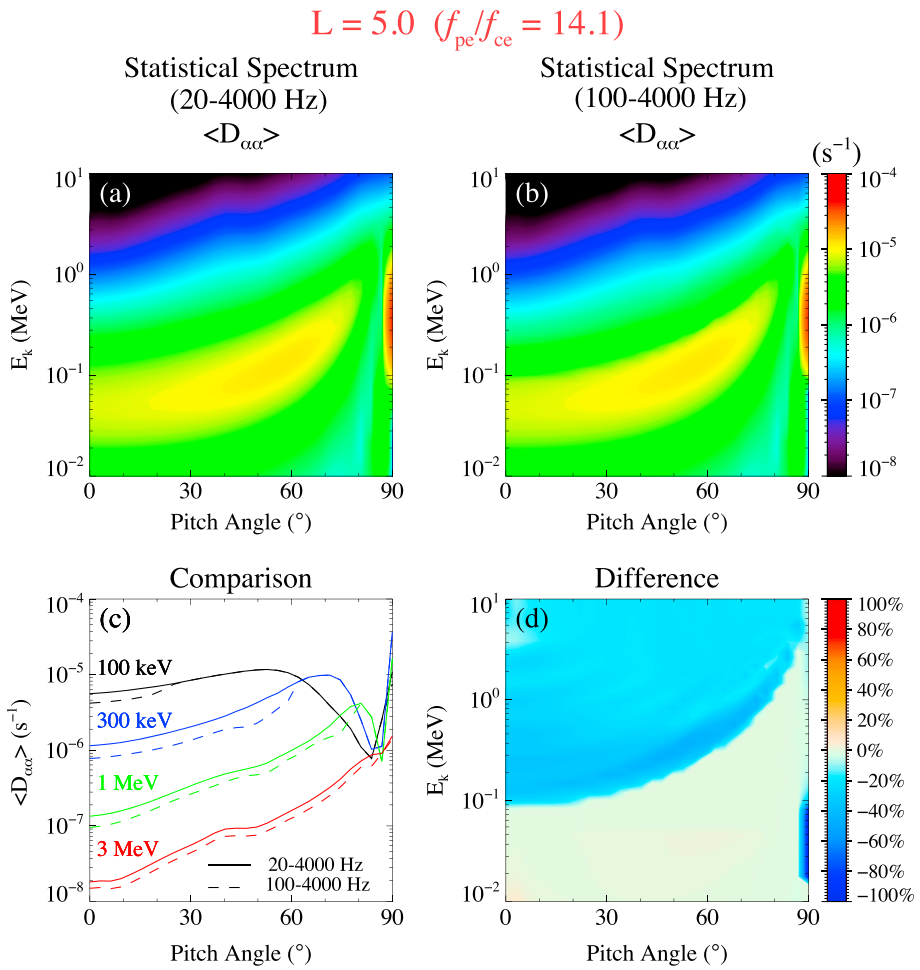

Figure 9. (a) Bounce-averaged pitch angle diffusion coefficients as a function of equatorial pitch angle and energy calculated by using the statistical wave spectrum over 20–4000 Hz at $L = 5$, where equatorial f_{pe}/f_{ce} is 14.1. (b) The same as Figure 9a but using the statistical spectrum over 100–4000 Hz by excluding the wave power below 100 Hz. (c) Pitch angle diffusion coefficients as a function of equatorial pitch angle for various energies (color coded) for the statistical spectrum over 20–4000 Hz (solid line) and 100–4000 Hz (dashed line). (d) The normalized difference of pitch angle diffusion coefficients $\frac{D_{\alpha\alpha}|_{100-4000\,\mathrm{Hz}} - D_{\alpha\alpha}|_{20-4000\,\mathrm{Hz}}}{D_{\alpha\alpha}|_{20-4000\,\mathrm{Hz}}}$ shown as a function of equatorial pitch angle and energy.

differences up to a factor of ~5. Therefore, it is important to incorporate this new statistical hiss wave frequency spectrum into the evaluation of hiss-driven electron precipitation.

We also calculate the bounce-averaged pitch angle diffusion coefficients driven by plasmaspheric hiss for our new statistical wave spectrum over 20–4000 Hz ($D_{\alpha\alpha}|_{20-4000\,\mathrm{Hz}}$) and a modified spectrum over 100–4000 Hz ($D_{\alpha\alpha}|_{100-4000\,\mathrm{Hz}}$) and show their comparison in Figure 9. We note that Figure 9a is exactly the same as Figure 8b. It is also important to note that the modified spectrum is the same as our new statistical spectrum but with a lower cutoff frequency at 100 Hz (instead of 20 Hz) to evaluate the role of the low-frequency hiss (<100 Hz) in electron scattering rates, which was not included in the CRRES statistics [e.g., *Meredith et al.*, 2007, 2009]. Since hiss wave intensity below <100 Hz is much weaker at lower L shells (≤3), as shown in Figure 6, the difference between $D_{\alpha\alpha}|_{20-4000\,\mathrm{Hz}}$ and $D_{\alpha\alpha}|_{100-4000\,\mathrm{Hz}}$ is negligible (not shown). However, at large L shells (≥4), low-frequency hiss wave intensity becomes more pronounced (Figure 6). As shown in Figure 9, at $L = 5$, $D_{\alpha\alpha}|_{20-4000\,\mathrm{Hz}}$ is larger than $D_{\alpha\alpha}|_{100-4000\,\mathrm{Hz}}$ by a factor of ~1.5 at energies above ~100 keV. Although the difference in pitch angle diffusion rates using statistically averaged hiss wave frequency spectra with and without including wave power below 100 Hz does not seem to be significantly large, this difference could be more pronounced when the peak wave frequency of hiss falls below 100 Hz [e.g., *Li et al.*, 2013; *Ni et al.*, 2014].

5. Summary and Discussion

Using 2 years of Van Allen Probes wave data, we constructed a new statistical model of hiss wave intensity and wave frequency spectrum over the frequency range of 20–4000 Hz, which is sufficient to cover the majority of hiss wave power. Statistical results of the hiss wave intensity distribution on a global scale show that hiss wave amplitudes are dependent on substorm activity (*AL**) with stronger (weaker) wave amplitudes occurring together with increasing levels of substorm activity on the dayside (nightside). Our new statistical hiss wave frequency spectrum deviates significantly from the frequently used Gaussian spectrum which is assumed to have a peak frequency at 550 Hz and frequency width of 300 Hz; statistical hiss peak frequencies are typically between 100 and 300 Hz with smaller values at larger *L* shells, which is generally consistent with the CRRES statistical results [*Meredith et al.*, 2007, 2009]. Importantly, hiss wave intensities extend well below ~100 Hz, which has been previously used as the lower cutoff frequency. Low-frequency hiss ($<$100 Hz) is preferentially observed during modest-to-strong substorm activity and tends to occur at larger *L* shells ($>$ ~3) on the dayside (04:00–16:00 MLT).

We also evaluated the differences in electron pitch angle diffusion coefficients using three different hiss wave frequency spectra: (1) the Gaussian spectrum with the peak frequency at 550 Hz and the frequency bandwidth of 300 Hz, (2) the new statistical spectrum from Van Allen Probes measurements, and (3) the same as (2) but excluding wave power below 100 Hz. Calculation results show that the difference is dependent on electron energy and *L* shell. Pitch angle diffusion coefficient from the new statistical result at $L = 3$ is a factor of $>$ ~5 larger at tens of keV, a factor of ~3 smaller over 70–200 keV, and a factor of ~2 larger over 0.3–1 MeV compared to the Gaussian spectrum. At a larger *L* shell of 5, although the pattern of the differences is similar, it shifts to lower energies. The new statistical wave frequency spectrum including wave power below 100 Hz typically leads to increases in pitch angle diffusion coefficients by a factor of ~1.5 for electrons with energies above ~100 keV at $L = 5$, but its effect is insignificant at $L \leq 3$.

Since realistic hiss wave frequency spectra are critical in evaluating pitch angle scattering rates inside the Earth's plasmasphere and plumes and the new statistical hiss wave frequency spectrum is quite different from the frequently adopted Gaussian frequency spectrum, we strongly suggest that the new and more realistic hiss wave frequency spectrum should be incorporated into future modeling of hiss-driven electron dynamics in the Earth's radiation belts.

Acknowledgments

This work was supported by JHU/APL contracts 967399 and 921647 under NASA's prime contract NAS5-01072. The analysis at UCLA was supported by EMFISIS subaward 1001057397:01; ECT subaward 13–041; NASA grants NNX11AD75G, NNX11AR64G, NNX13AI61G, NNX15AI96G, NNX14AI18G, and NNX15AF61G; and NSF grant AGS 1405054. We acknowledge the Van Allen Probes data from EMFISIS obtained from https://emfisis.physics.uiowa.edu/data/index.

Larry Kepko thanks Nigel Meredith and another reviewer for their assistance in evaluating this paper.

References

Abel, B., and R. M. Thorne (1998a), Electron scattering loss in Earth's inner magnetosphere: 1. Dominant physical processes, *J. Geophys. Res.*, *103*(A2), 2385–2396, doi:10.1029/97JA02919.

Abel, B., and R. M. Thorne (1998b), Electron scattering loss in Earth's inner magnetosphere: 2. Sensitivity to model parameters, *J. Geophys. Res.*, *103*(A2), 2397–2407, doi:10.1029/97JA02920.

Agapitov, O., A. Artemyev, V. Krasnoselskikh, Y. V. Khotyaintsev, D. Mourenas, H. Breuillard, M. Balikhin, and G. Rolland (2013), Statistics of whistler-mode waves in the outer radiation belt: Cluster STAFF-SA measurements, *J. Geophys. Res. Space Physics*, *118*, 3407–3420, doi:10.1002/jgra.50312.

Baker, D. N., et al. (2013), A long-lived relativistic electron storage ring embedded in Earth's outer Van Allen belt, *Science*, *340*(6129), 186–190, doi:10.1126/science.1233518.

Bortnik, J., R. M. Thorne, and N. P. Meredith (2007), Modeling the propagation characteristics of chorus using CRRES suprathermal electron fluxes, *J. Geophys. Res.*, *112*, A08204, doi:10.1029/2006JA012237.

Bortnik, J., R. M. Thorne, and N. P. Meredith (2008), The unexpected origin of plasmaspheric hiss from discrete chorus emissions, *Nature*, *452*, 62–66, doi:10.1038/nature06741.

Bortnik, J., W. Li, R. M. Thorne, V. Angelopoulos, C. Cully, J. Bonnell, O. Le Contel, and A. Roux (2009), An observation linking the origin of plasmaspheric hiss to discrete chorus emissions, *Science*, *324*(5928), 775, doi:10.1126/science.1171273.

Bortnik, J., L. Chen, W. Li, R. M. Thorne, N. P. Meredith, and R. B. Horne (2011), Modeling the wave power distribution and characteristics of plasmaspheric hiss, *J. Geophys. Res.*, *116*, A12209, doi:10.1029/2011JA016862.

Burtis, W. J., and R. A. Helliwell (1969), Banded chorus—A new type of VLF radiation observed in the magnetosphere by OGO 1 and OGO 3, *J. Geophys. Res.*, *74*(11), 3002–3010, doi:10.1029/JA074i011p03002.

Burton, R. K., and R. E. Holzer (1974), The origin and propagation of chorus in the outer magnetosphere, *J. Geophys. Res.*, *79*(7), 1014–1023, doi:10.1029/JA079i007p01014.

Chan, K.-W., and R. E. Holzer (1976), ELF hiss associated with plasma density enhancements in the outer magnetosphere, *J. Geophys. Res.*, *81*(13), 2267–2274, doi:10.1029/JA081i013p02267.

Chen, L., W. Li, J. Bortnik, and R. M. Thorne (2012), Amplification of whistler-mode hiss inside the plasmasphere, *Geophys. Res. Lett.*, *39*, L08111, doi:10.1029/2012GL051488.

Chen, L., et al. (2014), Generation of unusually low frequency plasmaspheric hiss, *Geophys. Res. Lett.*, *41*, 5702–5709, doi:10.1002/2014GL060628.

Dunckel, N., and R. A. Helliwell (1969), Whistler-mode emissions on the OGO 1 satellite, *J. Geophys. Res.*, *74*(26), 6371–6385, doi:10.1029/JA074i026p06371.

Glauert, S. A., R. B. Horne, and N. P. Meredith (2014), Three-dimensional electron radiation belt simulations using the BAS Radiation Belt Model with new diffusion models for chorus, plasmaspheric hiss, and lightning-generated whistlers, *J. Geophys. Res. Space Physics*, *119*, 268–289, doi:10.1002/2013JA019281.

Horne, R. B., R. M. Thorne, S. A. Glauert, N. P. Meredith, D. Pokhotelov, and O. Santolík (2007), Electron acceleration in the Van Allen radiation belts by fast magnetosonic waves, *Geophys. Res. Lett.*, *34*, L17107, doi:10.1029/2007GL030267.

Kletzing, C. A., et al. (2013), The Electric and Magnetic Field Instrument Suite and Integrated Science (EMFISIS) on RBSP, *Space Sci. Rev.*, *179*, 127–181, doi:10.1007/s11214-013-9993-6.

Kurth, W. S., S. De Pascuale, J. B. Faden, C. A. Kletzing, G. B. Hospodarsky, S. Thaller, and J. R. Wygant (2015), Electron densities inferred from plasma wave spectra obtained by the Waves instrument on Van Allen Probes, *J. Geophys. Res. Space Physics*, *120*, 904–914, doi:10.1002/2014JA020857.

Li, W., R. M. Thorne, V. Angelopoulos, J. Bortnik, C. M. Cully, B. Ni, O. LeContel, A. Roux, U. Auster, and W. Magnes (2009), Global distribution of whistler-mode chorus waves observed on the THEMIS spacecraft, *Geophys. Res. Lett.*, *36*, L09104, doi:10.1029/2009GL037595.

Li, W., R. M. Thorne, J. Bortnik, Y. Nishimura, V. Angelopoulos, L. Chen, J. P. McFadden, and J. W. Bonnell (2010), Global distributions of suprathermal electrons observed on THEMIS and potential mechanisms for access into the plasmasphere, *J. Geophys. Res.*, *115*, A00J10, doi:10.1029/2010JA015687.

Li, W., J. Bortnik, R. M. Thorne, and V. Angelopoulos (2011), Global distribution of wave amplitudes and wave normal angles of chorus waves using THEMIS wave observations, *J. Geophys. Res.*, *116*, A12205, doi:10.1029/2011JA017035.

Li, W., et al. (2013), An unusual enhancement of low-frequency plasmaspheric hiss in the outer plasmasphere associated with substorm-injected electrons, *Geophys. Res. Lett.*, *40*, 3798–3803, doi:10.1002/grl.50787.

Li, W., et al. (2014), Quantifying hiss-driven energetic electron precipitation: A detailed conjunction event analysis, *Geophys. Res. Lett.*, *41*, 1085–1092, doi:10.1002/2013GL059132.

Li, W., L. Chen, J. Bortnik, R. M. Thorne, V. Angelopoulos, C. A. Kletzing, W. S. Kurth, and G. B. Hospodarsky (2015), First evidence for chorus at a large geocentric distance as a source of plasmaspheric hiss: Coordinated THEMIS and Van Allen Probes observation, *Geophys. Res. Lett.*, *42*, 241–248, doi:10.1002/2014GL062832.

Lyons, L. R., and R. M. Thorne (1973), Equilibrium structure of radiation belt electrons, *J. Geophys. Res.*, *78*(13), 2142–2149, doi:10.1029/JA078i013p02142.

Lyons, L. R., R. M. Thorne, and C. F. Kennel (1972), Pitch-angle diffusion of radiation belt electrons within the plasmasphere, *J. Geophys. Res.*, *77*(19), 3455–3474, doi:10.1029/JA077i019p03455.

Mauk, B. H., N. J. Fox, S. G. Kanekal, R. L. Kessel, D. G. Sibeck, and A. Ukhorskiy (2012), Science objectives and rationale for the Radiation Belt Storm Probes mission, *Space Sci. Rev.*, 1–15, doi:10.1007/s11214-012-9908-y.

McPherron, R. L., D. N. Baker, T. I. Pulkkinen, T.-S. Hsu, J. Kissinger, and X. Chu (2013), Changes in solar wind-magnetosphere coupling with solar cycle, season, and time relative to stream interfaces, *J. Atmos. Sol. Terr. Phys.*, *99*, 1–13.

Meredith, N. P., R. B. Horne, R. M. Thorne, and R. R. Anderson (2003), Favored regions for chorus-driven electron acceleration to relativistic energies in the Earth's outer radiation belt, *Geophys. Res. Lett.*, *30*(16), 1871, doi:10.1029/2003GL017698.

Meredith, N. P., R. B. Horne, R. M. Thorne, D. Summers, and R. R. Anderson (2004), Substorm dependence of plasmaspheric hiss, *J. Geophys. Res.*, *109*, A06209, doi:10.1029/2004JA010387.

Meredith, N. P., R. B. Horne, S. A. Glauert, R. M. Thorne, D. Summers, J. M. Albert, and R. R. Anderson (2006), Energetic outer zone electron loss timescales during low geomagnetic activity, *J. Geophys. Res.*, *111*, A05212, doi:10.1029/2005JA011516.

Meredith, N. P., R. B. Horne, S. A. Glauert, and R. R. Anderson (2007), Slot region electron loss timescales due to plasmaspheric hiss and lightning-generated whistlers, *J. Geophys. Res.*, *112*, A08214, doi:10.1029/2007JA012413.

Meredith, N. P., R. B. Horne, S. A. Glauert, D. N. Baker, S. G. Kanekal, and J. M. Albert (2009), Relativistic electron loss timescales in the slot region, *J. Geophys. Res.*, *114*, A03222, doi:10.1029/2008JA013889.

Meredith, N. P., R. B. Horne, A. Sicard-Piet, D. Boscher, K. H. Yearby, W. Li, and R. M. Thorne (2012), Global model of lower band and upper band chorus from multiple satellite observations, *J. Geophys. Res.*, *117*, A10225, doi:10.1029/2012JA017978.

Ni, B., R. M. Thorne, Y. Y. Shprits, and J. Bortnik (2008), Resonant scattering of plasma sheet electrons by whistler-mode chorus: Contribution to diffuse auroral precipitation, *Geophys. Res. Lett.*, *35*, L11106, doi:10.1029/2008GL034032.

Ni, B., J. Bortnik, R. M. Thorne, Q. Ma, and L. Chen (2013), Resonant scattering and resultant pitch angle evolution of relativistic electrons by plasmaspheric hiss, *J. Geophys. Res. Space Physics*, *118*, 7740–7751, doi:10.1002/2013JA019260.

Ni, B., et al. (2014), Resonant scattering of energetic electrons by unusual low-frequency hiss, *Geophys. Res. Lett.*, *41*, 1854–1861, doi:10.1002/2014GL059389.

Parrot, M., and F. Lefeuvre (1986), Statistical study of the propagation characteristics of ELF hiss observed on GEOS 1, inside and outside the plasmasphere, *Ann. Geophys.*, *4*, 363–384.

Santolík, O., M. Parrot, L. R. O. Storey, J. S. Picket, and D. A. Gurnett (2001), Propagation analysis of plasmaspheric hiss using Polar PWI measurements, *Geophys. Res. Lett.*, *28*(6), 1127–1130, doi:10.1029/2000GL012239.

Santolík, O., M. Parrot, and F. Lefeuvre (2003), Singular value decomposition methods for wave propagation analysis, *Radio Sci.*, *38*(1), 1010, doi:10.1029/2000RS002523.

Sheeley, B. W., M. B. Moldwin, H. K. Rassoul, and R. R. Anderson (2001), An empirical plasmasphere and trough density model: CRRES observations, *J. Geophys. Res.*, *106*(A11), 25,631–25,641, doi:10.1029/2000JA000286.

Shprits, Y. Y., D. Subbotin, and B. Ni (2009), Evolution of electron fluxes in the outer radiation belt computed with the VERB code, *J. Geophys. Res.*, *114*, A11209, doi:10.1029/2008JA013784.

Summers, D., B. Ni, and N. P. Meredith (2007), Timescales for radiation belt electron acceleration and loss due to resonant wave-particle interactions: 2. Evaluation for VLF chorus, ELF hiss, and electromagnetic ion cyclotron waves, *J. Geophys. Res.*, *112*, A04207, doi:10.1029/2006JA011993.

Summers, D., B. Ni, N. P. Meredith, R. B. Horne, R. M. Thorne, M. B. Moldwin, and R. R. Anderson (2008), Electron scattering by whistler-mode (ELF) hiss in plasmaspheric plumes, *J. Geophys. Res.*, *113*, A04219, doi:10.1029/2007JA012678.

Thorne, R. M., E. J. Smith, R. K. Burton, and R. E. Holzer (1973), Plasmaspheric hiss, *J. Geophys. Res.*, *78*(10), 1581–1596, doi:10.1029/JA078i010p01581.

Thorne, R. M., et al. (2013), Evolution and slow decay of an unusual narrow ring of relativistic electrons near $L \sim 3.2$ following the September 2012 magnetic storm, *Geophys. Res. Lett.*, *40*, 3507–3511, doi:10.1002/grl.50627.

Tsurutani, B. T., and E. J. Smith (1974), Postmidnight chorus: A substorm phenomenon, *J. Geophys. Res.*, *79*(1), 118–127, doi:10.1029/JA079i001p00118.

Tsurutani, B. T., and E. J. Smith (1977), Two types of magnetospheric ELF chorus and their substorm dependences, *J. Geophys. Res.*, *82*(32), 5112–5128, doi:10.1029/JA082i032p05112.

Tsurutani, B. T., et al. (2006), Corotating solar wind streams and recurrent geomagnetic activity: A review, *J. Geophys. Res.*, *111*, A07S01, doi:10.1029/2005JA011273.

Tsurutani, B. T., B. J. Falkowski, J. S. Pickett, O. Santolik, and G. S. Lakhina (2015), Plasmaspheric hiss properties: Observations from Polar, *J. Geophys. Res. Space Physics*, *120*, 414–431, doi:10.1002/2014JA020518.

Tsyganenko, N. A., and M. I. Sitnov (2005), Modeling the dynamics of the inner magnetosphere during strong geomagnetic storms, *J. Geophys. Res.*, *110*, A03208, doi:10.1029/2004JA010798.